Inorganic Chemistry

Article

pubs.acs.org/IC

The μ_3 Model of Acids and Bases: Extending the Lewis Theory to Intermetallics

Timothy E. Stacey and Daniel C. Fredrickson*

Department of Chemistry, University of Wisconsin—Madison, 1101 University Avenue, Madison, Wisconsin 53706, United States

Supporting Information

ABSTRACT: A central challenge in the design of new metallic materials is the elucidation of the chemical factors underlying the structures of intermetallic compounds. Analogies to molecular bonding phenomena, such as the Zintl concept, have proven very productive in approaching this goal. In this Article, we extend a foundational concept of molecular chemistry to intermetallics: the Lewis theory of acids and bases. The connection is developed through the method of moments, as applied to DFT-calibrated Hückel calculations. We begin by illustrating that the third and fourth moments (μ_3 and μ_4) of the electronic density of states (DOS) distribution tune the properties of a pseudogap. μ_3 controls the balance of states above and below the DOS minimum, with μ_4 then determining the minimum's depth. In this way, μ_3 predicts an ideal occupancy for the DOS distribution. The μ_3-ideal electron count is used to forge a link between the reactivity of transition metals toward intermetallic phase formation, and that of Lewis acids and bases toward adduct formation. This is accomplished through a moments-based definition of acidity which classifies systems that are electron-poor relative to the μ_3-ideal as μ_3-acidic, and those that are electron-rich as μ_3-basic. The reaction of μ_3 acids and bases, whether in the formation of a Lewis acid/base adduct or an intermetallic phase, tends to neutralize the μ_3 acidity or basicity of the reactants. This μ_3-neutralization is traced to the influence of electronegativity differences at heteroatomic contacts on the projected DOS curves of the atoms involved. The role of μ_3-acid/base interactions in intermetallic phases is demonstrated through the examination of 23 binary phases forming between 3d metals, the stability range of the CsCl type, and structural trends within the Ti−Ni system.

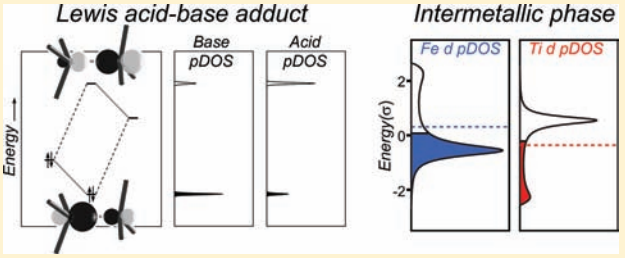

INTRODUCTION

The structural chemistry of intermetallic phases is expanding at a rate far exceeding the development of conceptual models for rationalizing this diversity or guiding their crystal structures. And yet, there are tantalizing hints that the same chemical factors as in molecular chemistry (the steric effects, electron counts, and electrostatic interactions that form the basic vocabulary of molecular stability and reactivity) are also at work in intermetallic structures.[1−24] These parallels are exemplified by the Zintl concept: the notion that when intermetallic phases form between elements with sufficiently large electronegativity differences, the resulting structures will attain closed-shell electron configurations on the atoms through ionization and covalent bond formation in accordance with the octet or Wade−Mingos rules.[25−27] Many intermetallics, however, lie outside of the Zintl phase family. Indeed, a fruitful area for exploratory synthesis has been the field of polar intermetallics,[28−35] in which combinations of elements with increasingly small electronegativity differences are probed, and the geometrically identifiable localized bonds of the Zintl phases vanish into a broad range of densely packed structures.

To illustrate the diversity of these phases (and the challenges of their analysis with theory), we show in Figure 1 a sampling of structures occurring in just one binary phase diagram: the technologically important Ti−Ni system.[36] Here, phases form

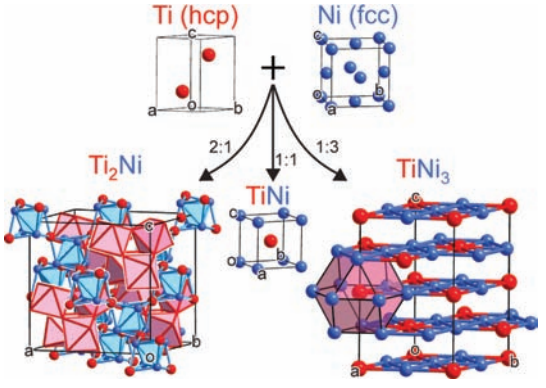

Figure 1. Structures of three binary phases in the Ti−Ni system: Ti_2Ni, TiNi (ht), and $TiNi_3$.

at three compositions: Ti_2Ni, TiNi, and $TiNi_3$.[37] TiNi adopts the CsCl type at temperatures above 170 °C (a lower-symmetry variant is obtained upon cooling),[38] while $TiNi_3$ forms as an ordered hcp/fcc intergrowth structure; both are variations on simple sphere packings with little hint of localized bonding. The Ti_2Ni phase crystallizes in a significantly more

Received: December 20, 2011
Published: March 15, 2012

   dx.doi.org/10.1021/ic202727k | Inorg. Chem. 2012, 51, 4250−4264

complex structure in which two substructures of diamond topology interpenetrate each other, one based on vertex-sharing stella quadrangula (blue), the other on face-sharing octahedra (pink). None of these structures can be rationalized using the Zintl concept.

For such intermetallic phases, the connections to molecular bonding schemes are far from mature, but tremendous progress has been made. Some of this progress has been conceptual, as in interpretation of the Bloch wave functions and band structures of periodic solids as extended molecular orbitals (MOs) and MO diagrams, respectively.[39−42] Other advances have been in our techniques for analyzing the output of electronic structure calculations in terms of chemical bonding. Examples include the development of the Crystal Orbital Overlap and Hamiltonian Populations (COOP and COHP),[43−45] the Electron Localization Function and Indicator (ELF and ELI),[46−50] and the bond critical point analysis component of the Quantum Theory of Atoms in Molecules (QTAIM).[51] The theoretical studies employing such techniques and others commonly associate structural stability with density of states (DOS) minima at the Fermi energy (E_F), reminiscent of the large HOMO−LUMO gaps of stable molecules, and often seen for the more polar Zintl phases. What underlies this connection?

In this Article, we will see that the notion of closed-shell configurations can be extended to these less-polar intermetallic phases. In moving away from the Zintl phases, however, we will need to abandon our focus on localized bonding features and pursue a connection to another concept in molecular bonding: the Lewis theory of acids and bases.[52,53] Using the Method of Moments and simple Hückel calculations (calibrated to attain quantitative agreement with DFT results), we will see that the elemental phases of the first-row transition metals can be naturally categorized according to how well their electronic DOS curves are suited to their electron counts, and that parallel features can be perceived in the electronic structures of Lewis acids and bases. In pursuing this connection, the diverse array of intermetallic structures formed by first row transition metals will emerge as a variety of acid−base adducts. In this picture, band gaps or pseudogaps emerge at the E_F in a process similar to the widening of the HOMO−LUMO gap during a Lewis acid−base interaction.

HOW MOMENTS SHAPE THE ELECTRONIC DOS

In seeing how acidity and basicity might extend to metal−metal interactions, we will need to take a different view of how geometry and electronic structure are connected than the association of electron counts with specific bonds or clusters. Such a connection is provided by the method of moments,[40,54−56] as applied to simple Hückel calculations.[57,58] The method of moments focuses on the relationships between the electronic density of states (DOS) distribution, and its moments

$$\mu_n = \int_{-\infty}^{\infty} E^n \mathrm{DOS}(E)\, \mathrm{d}E \tag{1}$$

which are quantities that measure various aspects of the distribution's shape.

For simple Hückel calculations, the moments of the DOS curve play the role of intermediary between the form of the DOS distribution and molecular geometry. The simplicity of the Hückel Hamiltonian allows for the moment μ_n to be expressed not only through the integral defined above (Figure 2, right), but also as a sum of products of Hamiltonian matrix elements (Figure 2, left). The latter equation corresponds to a

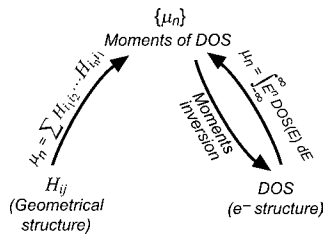

Figure 2. Link provided by the moments (μ_n) between the geometry of a structure and its simple Hückel density of states (DOS) distribution.

sum over closed n-fold paths of orbital interactions within a crystal structure, and allows for the μ_n values to be calculated from knowledge of the structure, without explicitly diagonalizing the Hamiltonian and calculating wave functions.

The ability to reconstruct a DOS curve from its moments values using any of a variety of moments inversion methods completes the bridge between geometry and the form of the DOS curve.[56,59−62] This bridge has been frequently applied to correlating differences of stability to the DOS moments, and ultimately to the structural features that underlie the differences in the moments.[63−67]

In this Article, we will apply the method of moments to a different question: For a given electron count, what are the optimal values of the moments of a DOS curve? The answer to this question is closely connected to how the moments relate to the shape of the DOS distribution. A DOS curve is, in fact, completely determined by its sequence of moments, $\{\mu_0, \mu_1, \mu_2, ..., \mu_\infty\}$.[56] While this is an infinite sequence, experience has shown that insights into the relative stabilities of competing structures can often be qualitatively assessed with only the five lowest order moments, μ_0−μ_4.[63,65−67] These low order moments will be the focus of this paper.

Of these low order moments, the first three, μ_0−μ_2 correspond to simple statistical quantities.[40] The zeroth order moment

$$\mu_0 = \int_{-\infty}^{\infty} \mathrm{DOS}(E)\, \mathrm{d}E \tag{2}$$

is simply the total area under the DOS curve. If this is normalized to 1, the first moment and second moments

$$\mu_1 = \int_{-\infty}^{\infty} E^1 \mathrm{DOS}(E)\, \mathrm{d}E \tag{3}$$

and

$$\mu_2 = \int_{-\infty}^{\infty} E^2 \mathrm{DOS}(E)\, \mathrm{d}E \tag{4}$$

become the average energy of the DOS distribution and the variance of the distribution around $E = 0$, respectively. In essence, μ_0−μ_2 correspond to properties for the x and y axes for the DOS plot: μ_0 sets the scale along the x-axis, μ_1 determines the location of the origin along the y-axis, and μ_2 controls the scale along the y-axis. Standardizing these values to $\mu_0 = 1$, $\mu_1 = 0$, and $\mu_2 = 1$ allows us to focus on the roles that higher-order moments play on the DOS shape. These adjustments mean that integrated DOS values range from 0 for an empty band structure to 1 for a completely filled one, while energies are

dx.doi.org/10.1021/ic202727k | Inorg. Chem. 2012, 51, 4250−4264

measured relative to the average for the DOS curve in units of the standard deviation for the distribution, σ, rather than more familiar units such as electronvolts or Hartrees.

The higher moments μ_3 and μ_4 determine more significant characteristics of the shape of the DOS curve. This is illustrated in Figure 3 with a sequence of DOS curves with differing values

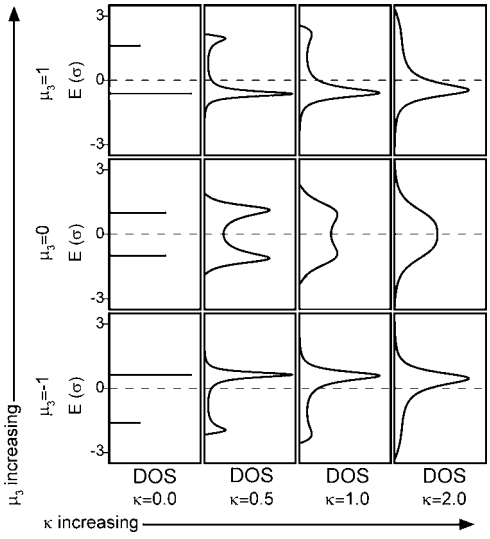

Figure 3. Influence of the third moment (μ_3) and kurtosis (κ) on the shape of a DOS distribution. A comparison of DOS curves with varying values of μ_3 and κ (but equal values for all lower moments) illustrates that μ_3 determines the balance in the numbers of states above and below a DOS gap or pseudogap, while κ controls how pronounced the gap is.

of these two moments. The curves are arranged in a 3 × 4 matrix, with the three rows showing series of curves with μ_3 values that are greater than, equal to, or less than zero. When μ_3 = 0 (middle panels), the DOS curve is symmetrically distributed around the average. As μ_3 shifts away from zero, the DOS curve begins to exhibit asymmetry. For $\mu_3 > 0$ (top panels), the bulk of DOS distribution moves below the average, with a small number of states moving to much higher energies to maintain the zero average energy. For $\mu_3 < 0$ (bottom panels), the reverse occurs with largest DOS peak now appearing above the average energy. In this way, μ_3 can then be seen to tune the balance between the numbers of low- and high-lying states.[67,68]

μ_4 plays a different role in shaping the DOS curve. This role, however, is obscured by the dependence that the raw fourth moment has on the preceding lower order moments.[67] As is discussed in ref 67, this dependence can be removed by taking a modified form of μ_4 known as kurtosis (κ): $\kappa = \mu_4 - \mu_3^2 - 1$ (when μ_0 through μ_2 are standardized; see ref 67 for the full unstandardized form). At a high κ value (right panels), the distributions appear as single broad peaks, with the degree of asymmetry about $E = 0$ being determined by μ_3. As the κ is lowered, the single broad peaks become resolved into a pair of increasingly narrow peaks, with a gap or pseudogap appearing between them.[67,68] At $\kappa = 0$, the DOS distribution reduces to a pair of δ-functions whose relative heights are determined by μ_3.[69]

In summary, μ_3 tunes the balance between the numbers of low energy and high energy states, while κ dictates the depth of a DOS minimum separating them. This can be rephrased in a simple, chemical fashion: μ_3 and κ dictate the character of a DOS gap or pseudogap. μ_3 determines its position, κ its depth.

OPTIMIZING μ_3 AND κ TO ELECTRON COUNT

The observation that μ_3 and κ control the position and depth of a DOS pseudogap suggests that these variables should be closely associated with stability of a phase as a function of electron count. This leads us to a simple question: For a given electron count, what are the optimal values of μ_3 and κ?[70] A pragmatic way of finding the best shape parameters is to choose an electron count and examine the ability of the DOS distribution to stabilize these electrons as a function of μ_3 and κ. This can be done with the following steps. First, we use a moments inversion scheme[60,71] to construct DOS curves for a series of μ_3 and κ values (for technical details see the Supporting Information). We then populate each of the DOS distributions to the prescribed band-filling, and compare their total energies (E_{tot}).

A vivid way of making this comparison is to plot E_{tot} as a function of μ_3 and κ, as is illustrated in Figure 4 with a contour

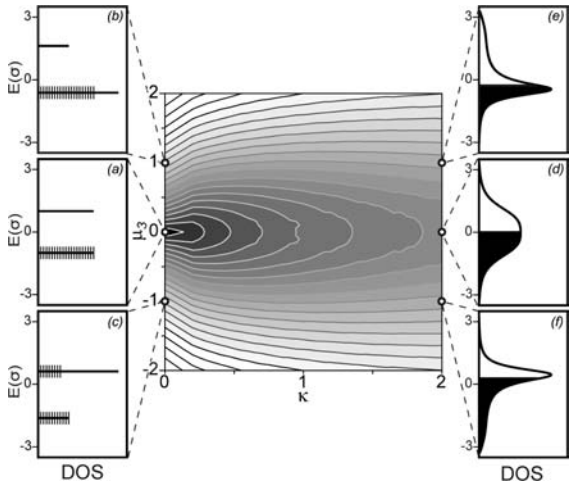

Figure 4. Total energy as a function of μ_3 and κ for a half-filled DOS distribution. The form of the DOS curve is given in the left and right margins for the points (a) $\mu_3 = 0$, $\kappa = 0$, (b) $\mu_3 > 0$, $\kappa = 0$, (c) $\mu_3 < 0$, $\kappa = 0$, (d) $\mu_3 = 0$, $\kappa > 0$, (e) $\mu_3 > 0$, $\kappa > 0$, and (f) $\mu_3 < 0$, $\kappa > 0$. The total energies in the plot range from −0.50 σ (black) to −0.10 σ (white).

map for a 50% band-filling. The landscape of the $E_{tot}(\mu_3, \kappa)$ function has a simple form: The map is dominated by a deep minimum (black) at the left of plot corresponding to the point $\mu_3 = 0.0$, $\kappa = 0.0$. The rest of the terrain funnels into this minimum.

The form of this contour map can be understood by inspecting the shape of the DOS distributions and the position of the E_F at a representative sample of points. At the global minimum (Figure 4a), the DOS curve consists of a symmetric pair of delta functions, as expected for $\mu_3 = 0$ and $\kappa = 0$. At the 50% occupation, the E_F lies between these peaks. This clear separation between low-energy filled states and high-energy empty ones is expected to be highly favorable.

Upon moving away from $\mu_3 = 0$ and $\kappa = 0$, the situation becomes less ideal. Increasing μ_3 past zero (Figure 4b) shifts the lower peak to a higher energy value as it accommodates a larger number of states while leaving μ_2 constant. The placement of E_F inside this peak is consistent with the fact that these additional low energy states have been left

dx.doi.org/10.1021/ic202727k | Inorg. Chem. 2012, 51, 4250−4264

unoccupied. Decreasing μ_3 below zero leads to a similarly inefficient distribution of states (Figure 4c). The shrinking of the low energy peak forces some electrons to occupy states in the upper peak.

Looking at how the results change as we move away from $\kappa = 0$ shows that κ plays a different role in determining stability. If we begin at the $\mu_3 = 0$, $\kappa = 0$ minimum, and increase κ (Figure 4d), the band gap shrinks as the higher- and lower-energy peaks broaden. This shrinkage forces some electrons to populate states at higher energy levels closer to the E_F, leading to an increase in E_{tot}. This is destabilizing, as is evident in the lightening of the colors of the contour map on moving from the minimum to the right. A different result, however, is obtained if we begin at μ_3 values away from the minimum. Along both the $\mu_3 = 1$ and -1 lines (Figure 4e,f), increased κ leads to a broadening of the partially occupied peak, with the occupied states at the bottom of that peak being stabilized with no energetic cost incurred by raising the energies of the unoccupied states at the top of the peak. Increased κ is now stabilizing, as can be seen in the darkening of the color on moving to the right along these lines.

The energetic consequences of the peak broadness governed by κ can now be inferred: Whereas μ_3 determines the optimal electron count for a distribution, κ tunes the magnitude of this preference. For $\kappa = 0$, the preference for the ideal electron count is sharpest, while moving to larger κ values dulls this preference.

These conclusions extend to other band-fillings (BFs). In Figure 5, we plot contours for a range of percent BF from 5% to

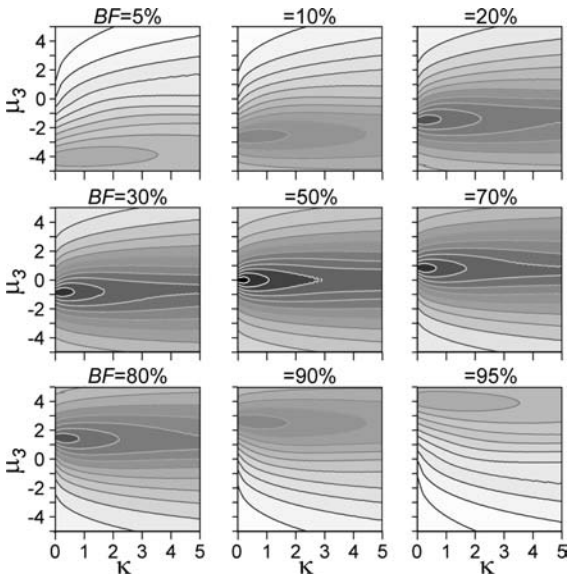

Figure 5. Total energy of a DOS curve as a function of μ_3 and κ at a series of band-filling (BF) values between 5% and 95%. Across the plots, the energies range from −0.50 (black) to −0.01 σ (white).

95%. These have similar appearances to that presented for BF = 50%, with each having a minimum along the $\kappa = 0$ line. However, the position of this minimum changes along the μ_3-axis with the value of BF. At BF = 5% the minimum occurs at about $\mu_3 = -4$. As BF is increased, the minimum ascends the μ_3-axis, passing through $\mu_3 = 0$ at BF = 50%, and reaching $\mu_3 = +4$ at BF = 95%. We also note that the minimum is relatively shallow at high and low occupancies, and becomes deepest at BF = 50%. This reflects the larger range of possible total energies for a half-filled DOS distribution than for nearly filled or vacant ones. Indeed, the corresponding surfaces for BF = 0% and 100% are flat.

From the contour plots in Figure 5 several clues to the question of the optimal μ_3 and κ values for a given electron count are evident. For each electron count a minimum appears in the $E_{tot}(\mu_3, \kappa)$ surface, corresponding to these optimal values. The μ_3 value of this minimum increases monotonically as the occupation is increased, and its κ value is always zero.

The observation that the minimum invariably occurs at $\kappa = 0$ leads to considerable simplification. With $\kappa = 0$, the DOS distribution simply consists of two δ-functions (Figure 6a). As

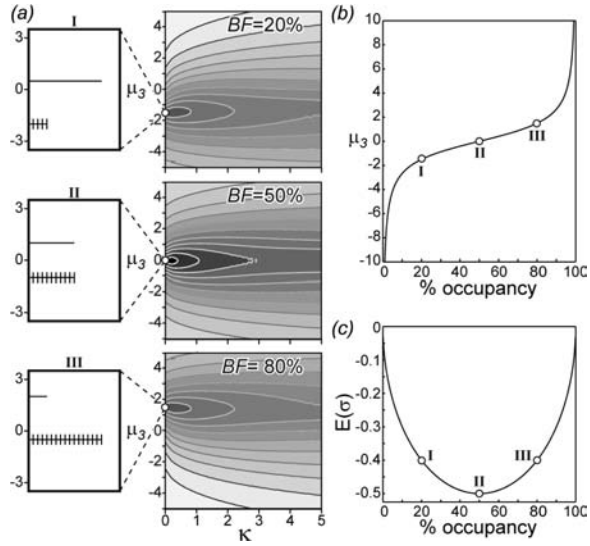

Figure 6. Solution to the question of the optimal μ_3 and κ values for a given band-filling (BF). (a) The DOS curves corresponding to the minima in the total energy function, $E_{tot}(\mu_3, \kappa)$, for a series of BF values. In all cases the minimum occurs at $\kappa = 0$, with the μ_3 value increasing monotonically with the BF value. (b) Curve of the ideal μ_3 values for a DOS distribution as function of BF. (c) The E_{tot} value at the minimum as a function of BF. Roman numerals mark corresponding points in the three panels.

is demonstrated in the Supporting Information, the minimum E_{tot} is obtained for the μ_3 value that makes the fraction of states in the lower DOS peak equal to BF so that the E_F separates the two peaks. In the process of proving this intuitive result, equations emerge relating the BF to the μ_3 and E_{tot} values at the minimum:

$$\mu_3 = \frac{2\mathrm{BF} - 1}{(\mathrm{BF} - \mathrm{BF}^2)^{1/2}} \quad (5)$$

$$E_{tot} = -(\mathrm{BF} - \mathrm{BF}^2)^{1/2} \quad (6)$$

These equations encode simple relationships between BF and the ideal values of μ_3 and E_{tot} as is shown with graphs in Figure 6b,c, respectively. The curve of optimal μ_3 shows a monotonic increase in μ_3 with BF, with μ_3 reaching $-\infty$ and $+\infty$ at the limits of BF = 0% and 100%, respectively, and a slightly upward-running linear region at intermediate BF values. The curve provides a direct translation between BF and its ideal

dx.doi.org/10.1021/ic202727k | Inorg. Chem. 2012, 51, 4250−4264

μ_3 value. In fact, one can reverse the relationship to obtain the ideal BF as a function of μ_3:

$$\mathrm{BF} = \frac{1}{2} + \frac{\mu_3}{2\sqrt{\mu_3^2 + 4}} \quad (7)$$

From this equation, the monotonic increase of the ideal BF with μ_3, and its value of $^1/_2$ at $\mu_3 = 0$ can be confirmed.

The connection between BF and E_{tot} has a similarly uncomplicated form. A plot of the ideal total energy as a function of BF is shown in Figure 6b. The plot has the shape of the letter "U" or half-pipe skateboard ramp with E_{tot} being zero at the filled and empty limits, and ballooning downward to a rounded minimum at 50% occupancy. This shape represents the strong potential for bonding stabilization for half-filled systems of orbitals, and the absence of bonding stabilization for completely filled or empty systems.

With the above equations and the plots in Figure 6, we have come to a solution of the question of the optimal values of the μ_0–μ_4 moments for a given electron count. The optimal μ_3 value is strongly dependent on the electron count, and increases from $-\infty$ to $+\infty$ as the DOS distribution is populated. The ideal κ value, on the other hand, is uniformly zero. This leads to the largest possible band gap between filled and unfilled levels.

These results yield predictions of the optimal μ_3 for the electron count of a phase. When are these predictions expected to be obeyed by experimentally observed compounds? A look through the DOS curves in the figures above helps answer this question. Curves generated from the moments μ_0–μ_4 have a limited range of forms, extending from single broad peaks (high κ) to sharp bimodal distributions (low κ). Additional flexibility is provided by the possibility of the curve being either nearly symmetric (small $|\mu_3|$) or asymmetric (large $|\mu_3|$). A low-order moment model of this form will thus not be able to reproduce the DOS distribution for a complicated system involving interactions between orbitals centered at many different energy levels.

Instead, this method would be expected to apply best to a system with a very limited basis set of valence orbitals whose interactions lead to a distinct set of bonding and antibonding levels. The success of the above analysis in predicting μ_3 values from electron count or vice versa will depend on our ability to isolate the essential orbital interactions underlying stability. We will see in the following that such severe simplifications lead to a surprisingly fruitful view of bonding in intermetallic phases.

μ_3 OPTIMIZATION IN THE ELEMENTAL PHASES OF THE TRANSITION METALS

With the relationships between the electron count populating a DOS curve and the curve's ideal values for μ_3 and κ in hand, we can now evaluate how well the electronic structures of metals and intermetallics achieve these ideal moment values. As we described above, the predictions of the low-order moment model are expected to be best obeyed by systems governed by interactions between valence orbitals centered over a narrow range of energies. Such are provided by the transition metal elements, whose DOS curves are dominated by a relatively dense block of states arising from the valence d orbitals. Indeed, in one of the early applications of the Method of Moments, Burdett and Lee demonstrated that the trend in the preferences for close-packed (hcp or fcc) versus bcc structures for the d-block of the periodic table could be well-reproduced with a d-orbital-only model using moments up to μ_4.[63] Other studies have shown that the d-valence shell is the most important for determining the geometrical structure of transition metal alloys.[72,73] The precedents for using a d-only model for understanding the electronic structure of transition metal alloys also extend to surface chemistry.[74]

How well are the moments values for the DOS curves of the elemental phases of the transition metals optimized for their electron counts? To answer this, we perform Hückel calculations on each of the 3d metals using an spd basis set, the parameters of which are optimized against the results of GGA-DFT calculations.[75,76] We then read the occupancy of the 3d orbitals for each phase (consistently near the total number of valence electrons minus one electron/atom for the sp states, as assumed in ref 63), and truncate the Hückel calculations to a d-only, low order moment model as follows: we first extract the Hamiltonian matrix elements (H_{ij}'s) for interactions among the 3d orbitals. From these sets of H_{ij}'s we then calculate the standardized μ_3 and κ for each phase, and construct approximate DOS curves from these values. Finally, we populate the resulting DOS distribution to the 3d orbital occupancy from the full Hückel calculations to obtain an approximate total energy for the system of d orbitals.

The results of this analysis are presented in Figure 7. The total energies obtained for each of the 3d elements are

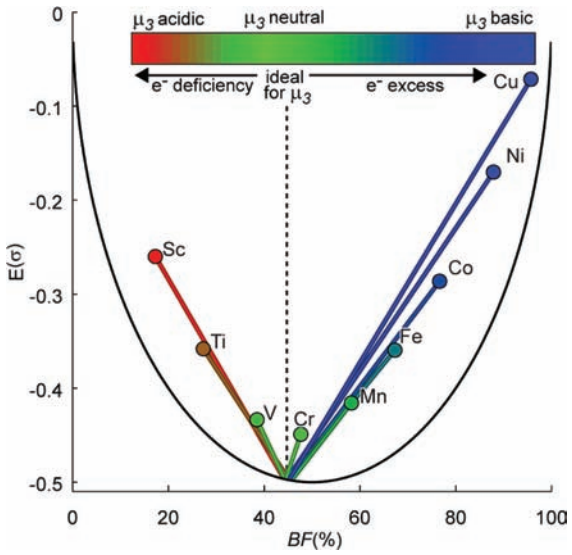

Figure 7. Plot of the μ_0–μ_4, d-only total energy (E_{tot}) versus band-filling (BF) for the first row transition metals Sc–Cu in their elemental phases relative to the ideal values (black curve). From each (BF, E_{tot}) point a line is drawn to the position on the ideal curve corresponding to the optimal E_{tot} and BF calculated from the μ_3 of the DOS curve for that atom. Color is used to indicate the degree of μ_3 acidity for each site: red for acidic (electron-poor relative to the ideal electron count), green for neutral (electron count approximately equal to ideal), and blue for basic (electron-rich relative to the ideal).

represented with dots plotted along with the curve of ideal total energies versus band-filling, the "U"-shaped curve of Figure 6c. The point corresponding to each element hovers above the curve of ideal values, and the sequence of points on going from left to right on the periodic table roughly follows the shape of the curve. The placement of the points at higher energy than the ideal value is not unexpected: the ideal values correspond to DOS curves built from two δ-functions. This is far from realized

dx.doi.org/10.1021/ic202727k | Inorg. Chem. 2012, 51, 4250–4264

in metallic systems; the κ value for these phases is expected to be universally higher than ideal.

μ_3 turns out to be an easier parameter to optimize. In Figure 7, we represent the deviation of the μ_3 value for a phase from its the ideal value in the following way: we draw a line connecting a phase's (BF, E_{tot}) point to the point on the ideal curve predicted by the μ_3 value. The component of that line along the BF-axis then gives the difference between the actual and ideal BF values for that element.

The resulting lines in Figure 7 create a "V"-shaped pattern. The V's point represents an ideal occupancy of about 44% shared by all of these elements, despite the differences in crystal structures that occur across the series (Sc−Ti are hcp; V, Cr, and Fe are bcc; Co−Cu are fcc; Mn prefers the more complex α-Mn type under ambient conditions[77]). As the ideal occupancy is essentially fixed, the actual occupancies exhibit different degrees of mismatch from this ideal over the row of the periodic table. At the farthest left, the elements are electron deficient relative to the ideal, while those at the right have an excess of electrons. Near the middle of the series at V and Cr, the elements are very close to realizing the optimal electron count.

μ_3-ACIDS AND BASES: GENERALIZING THE LEWIS THEORY

From the distribution of (BF, E_{tot}) in Figure 7, we may conclude that there is little correlation between the μ_3 values for the elemental phases and their electron counts. But what about their reactivities? The placement of the actual BF values for Sc and Ti to the left of the ideal value suggests that these elements could gain stability by either gaining electrons or engaging in new interactions that tune their μ_3 values to accommodate their lower electron counts. In the same way, the placement of the (BF, E_{tot}) points for Mn−Cu to the right of the ideal electron count predicts that the mismatch in electron count could be soothed by the elements either losing electrons or engaging in interactions that raise the μ_3 value to better suit their higher electron counts.

The vocabulary of chemistry offers numerous terms for describing such electron-poor or -rich atoms, such as electron acceptors/donors or nucleophiles/electrophiles. Over the remainder of this Article, we will see with increasing clarity that an analogy to the concept of Lewis acids and bases is especially productive. Atoms such as Sc and Ti whose electron counts fall short of the μ_3 ideal are in a position to accept electrons like Lewis acids. We will refer to these as μ_3 acids. In a similar way, Mn−Cu, whose electron counts exceed the μ_3 ideal, are poised to donate electrons, just as are Lewis bases. We will call these μ_3 bases. V and Cr, whose electron counts closely approximate the ideal for their μ_3 values are then considered to be essentially μ_3 neutral.

In the Lewis theory of acids and bases, bases are defined as electron-pair donors, while acids are electron-pair acceptors.[78] These characteristics can usually be traced to the presence in the molecular orbital (MO) diagrams of the species of a high-lying occupied MO (for bases) or low-lying unoccupied MO (for acids) whose shape is poised for intermolecular interactions. The reaction between a Lewis base and an acid to form a stable adduct is dominated by the interaction between these frontier orbitals. In Figure 8, we illustrate this process schematically for the classic example of the formation of an adduct between NH_3 and BF_3.[79] The frontier orbitals for these two molecules are first sketched out separately in panel a, and

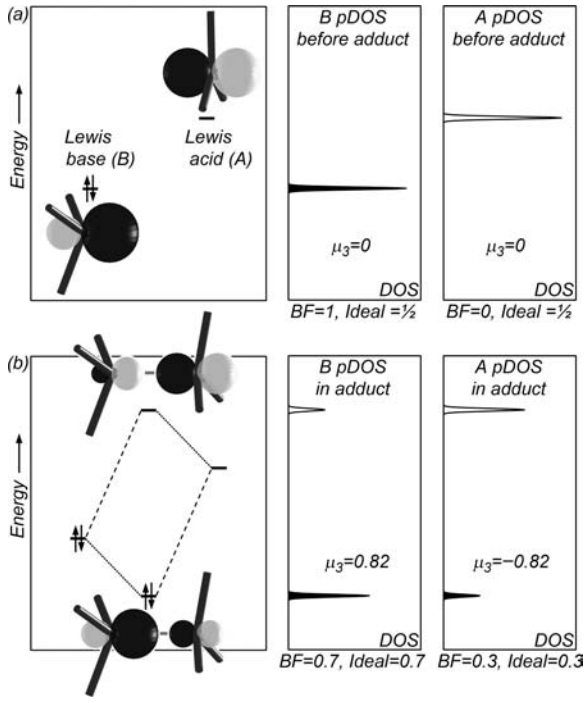

Figure 8. Lewis acids and bases as a specific case of μ_3 acids and bases. (a) A schematic view of the electron pair donor orbital of a Lewis base, the electron pair acceptor orbital of a Lewis acid, and their projected DOS (pDOS) curves. The fraction occupations (BFs) of the base and acid orbitals are too large and too small, respectively, relative to the ideal counts dictated by their μ_3 values. (b) Upon formation of a Lewis acid−base adduct, the shapes of the pDOS curves and the electron populations of the orbitals change to achieve an exact correspondence between the actual and μ_3-ideal BF values.

then their interaction to form bonding and antibonding MOs is shown in panel b. Here, the creation of a filled bonding orbital and a large HOMO−LUMO gap provides the standard account for the stability of this complex.

An alternative perspective can be obtained, however, if we follow the projected DOS curves for the Lewis base (B) and acid (A) orbitals, as well as their μ_3's, during this interaction. The DOS curves for orbitals A and B before adduct formation (Figure 8a) each appear as single δ-functions. The standardized μ_3 values for both are zero. This corresponds to an ideal BF value of $^1/_2$, i.e., one electron/orbital. This ideal BF is far from the actual occupations: the basic orbital B is occupied by an electron pair (BF = 1), while the acidic orbital A is empty (BF = 0). The shapes of the DOS curves for these two orbitals are clearly poorly optimized for their occupations.

This changes upon adduct formation. The μ_3 for orbital B is raised through the interaction of the higher energy A to help accommodate its electron excess. This shift in μ_3, in combination with some electron transfer to orbital A, leads to perfect consistency between the μ_3 value for orbital B and its electron count. The shape of the DOS distribution for orbital A is likewise optimized. Interaction with the lower energy orbital B to lower its μ_3 and the acceptance of electrons leads to a match between the μ_3 value and orbital occupation. The net result is that the DOS shapes for both B and A now consist of pairs of δ-functions, with the lower energy peak completely filled and the upper peak completely empty. These curves have achieved both the optimum μ_3 and κ for their occupations.

dx.doi.org/10.1021/ic202727k | Inorg. Chem. 2012, 51, 4250−4264

In the course of Lewis adduct formation, the reactivities of the acid and base are neutralized from the perspectives of both the Lewis and μ_3 models of acids and bases. As we will see in the coming sections, the moments-based interpretation of acidity advances the Lewis theory of acids and bases beyond simple electron-pair transfer to any interaction which better sculpts a DOS distribution to its occupancy. This view will be particularly applicable to the formation of intermetallic phases. In this translation between the Lewis and μ_3-based pictures of acidity, the large HOMO−LUMO gap of the Lewis adduct becomes the DOS pseudogap determined by μ_3 and κ.

μ_3-NEUTRALIZATION THROUGH BINARY PHASE FORMATION

The analogy between the electron deficiency or excess in transition metal elemental phases and the Lewis acid/base theory becomes productive in its implication of the possibility of "neutralization" reactions between μ_3-acidic and basic metals. As a first test of this idea, we now turn to binary phases formed between the most extreme cases in Figure 7: Sc and Cu, the atoms of which are 2.7 electrons under and 5 electrons over the μ_3 ideal, respectively. The Sc−Cu phase diagram exhibits several binary phases, an indication of favorable interactions between these elements: ScCu (CsCl-type), $ScCu_2$ ($MoSi_2$-type), and $ScCu_4$ (structure type unknown).

Let us begin with the simplest of these, the CsCl-type 1:1 phase (Figure 9a). Our procedure for analyzing this compound is similar to that described for the elemental phases above. We first perform a Hückel calculation on the ScCu phase with spd basis sets for both atoms (with Hückel parameters optimized to reproduce the GGA-DFT band structure and projected DOS curves of ScCu; see Supporting Information), and extract the occupancies of the d-orbitals for Sc and Cu. Next, we strip down the basis set to simply the Sc and Cu 3d orbitals, and calculate the μ_3 and κ values for both atoms. Finally, we construct approximate atomic DOS curves, populate them to obtain total energies, and compare the calculated and ideal E_{tot} values, as well as the actual and ideal band-fillings.

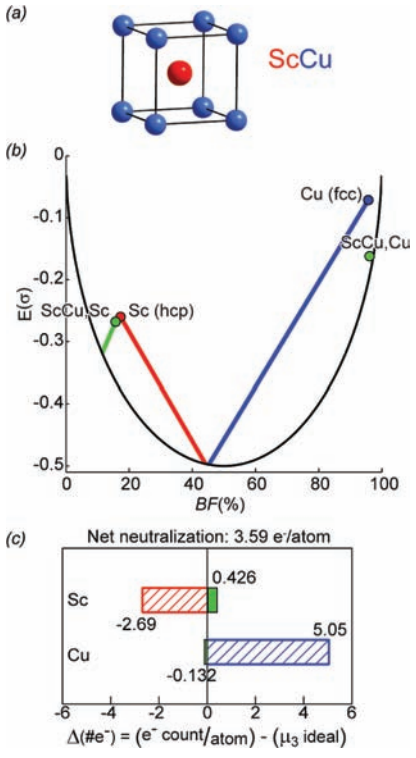

Figure 9. μ_3-acidity analysis of the formation of ScCu from its component elements. (a) The CsCl-type structure of ScCu. (b) A plot of (BF, E_{tot}) points from μ_0−μ_4 models for Sc and Cu atoms in their elemental phases and in ScCu relative to the ideal values (black curve). See caption to Figure 7 for plotting conventions and the significance of colors. (c) Bar graphs illustrating the deviation from the ideal electron counts calculated from the μ_3 for atoms of Sc and Cu in their elemental phases (hashed bars) and in ScCu (solid bars).

The results of this analysis are presented in Figure 9b, where (BF, E_{tot}) points for both Sc and Cu are connected to the positions on the ideal U-shaped curve predicted by their μ_3 values. The original points for the elemental phases are also given for comparison. Similarities and differences between the results for the binary and elemental phases are seen. In terms of similarities, the band-filling values for both Sc and Cu show little change on going from the elements to the intermetallic compound, indicating that at this approximate level of theory essentially no electron transfer has occurred between the d orbitals of Sc and Cu. In fact, a consistent feature of the Hückel calculations presented in this paper is that the d-orbital occupation for any given atom remains virtually constant on going from an elemental phase to an intermetallic. In this way, the low-order moment/d-orbital-only models yield largely covalent pictures of the bonding in these phases.

Differences occur in the other aspects of the graph. Whereas the μ_3 ideal BF values for elemental Sc and Cu are nearly equal at about 44%, a significant splitting arises in ScCu. The ideal BF for Sc has moved to the left all the way from 44% to 11%. This more than corrects for the electron deficiency calculated for elemental Sc. An even more significant change is seen in the ideal BF for Cu, from 44% to 97%. The ideal BF value now lies essentially under the Cu (BF, E_{tot}) point, such that consistency between electron count and μ_3 value has been achieved. Indeed, for both Cu and Sc, participation in the CsCl-type phase offers substantially improved agreement between the level of occupation of their d orbitals and their μ_3 values (and E_{tot} values closer to the ideal curve).

In Figure 9c, we show a more compact way of displaying these results. For both Sc and Cu, bars are drawn corresponding to the number of electrons in excess or deficiency relative to the ideal number calculated from the atomic μ_3. Bars filled with hashed lines give the electron count mismatch for the elemental phases, while those drawn with solid bars show the mismatch for the same element in the binary phase. Upon the formation of ScCu from its component elements, Sc goes from being deficient by 2.7 electrons/atom to having an electron excess of 0.4 electrons/atom. For Cu, the 5.05 electrons/atom excess of the elemental phase is relieved to a slight deficit of 0.13 electrons/atom in ScCu. During the reaction Sc + Cu → ScCu, the μ_3-acidic and basic characters of Sc and Cu, respectively, have transformed to being relatively μ_3-neutral. A quantitative measure of this change is the net neutralization per atom: the average decrease in the mismatch from the μ_3-ideal per atom on forming the intermetallic phase from its component elements. In the case of ScCu, the net neutralization is 3.59 electrons/atom.

As the basis of the μ_3 acidity concept lies in the third moment's control of the position of a DOS minimum, we may expect that μ_3-neutralization will inscribe a signature on the DOS curves, similar to the large HOMO−LUMO gap seen in

dx.doi.org/10.1021/ic202727k | Inorg. Chem. 2012, 51, 4250−4264

Lewis acid–base adducts. While this can indeed be seen for ScCu (see Supporting Information), the effect is more clear in the pairing of elements with less extreme μ_3 acidity and basicity, such as Ti and Fe. In Figure 10a, we plot the (BF, E_{tot}) values for Ti and Fe in the CsCl-type phase TiFe. The resulting graph shows features analogous to those obtained for ScCu: while Ti and Fe appear as a μ_3-acid and base, respectively, in their elemental phases, they achieve nearly perfect neutralization through the formation of the intermetallic phase.

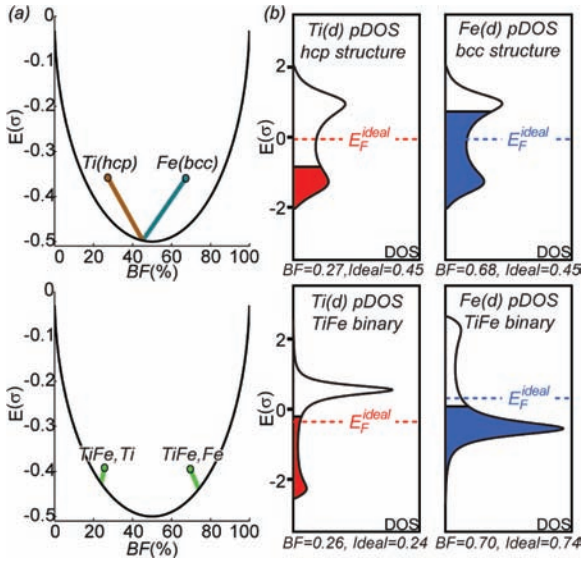

Figure 10. μ_3-Neutralization of TiFe in the CsCl-type. (a) Comparison of (BF, E_{tot}) points for Ti and Fe relative to their μ_3-ideals before and after forming the intermetallic. (b) The reconstructed DOS curves from the μ_3 and κ values for Ti and Fe before and after intermetallic phase formation. For each DOS curve, filled states are denoted with shading, and the Fermi energy corresponding to the ideal BF (E_F^{ideal}) is marked with a dashed line.

In Figure 10b, we show how changes in the model Ti and Fe 3d DOS curves underlie this neutralization. For the elemental phases, both Ti and Fe show bimodal DOS curves, with a DOS minimum roughly dividing the curves into equal parts. The ideal BF value of 44% gives a Fermi energy (dotted line) that lies right in the middle of this pseudogap. The actual occupancies of the bands (as indicated by the shaded regions) miss this ideal BF by substantial margins, with the Ti DOS distribution being under-filled relative to the ideal and that of Fe being overfilled. Upon forming the TiFe compound, the weight of the Ti DOS distribution shifts to higher energies, with only a small minority of states remaining under the pseudogap. A change in the opposite direction occurs for the Fe curve: the bulk of the Fe states now lie below the pseudogap. In this process, the Ti and Fe DOS curves adopt shapes more consistent with their low and high occupancy by electrons, respectively. The final curves are reminiscent of the projected DOS curves of the Lewis acid and base orbitals in the adduct of Figure 8, re-enforcing the analogy to the Lewis view of acids and bases.

ScCu and TiFe are but two members of a large family of intermetallic compounds formed between the first-row transition metal elements. In Figure 11, we show the results of applying this μ_3 acidity analysis to DFT-calibrated Hückel models for other members of this family. μ_3-Neutralization bar graphs are plotted for 17 phases chosen to span a wide range of electronegativity differences, as well as some of the structural diversity in this family.[37,80−116]

The phases are first grouped according to their μ_3 acid: Sc, Ti, or V. Each series is then arranged according to the total number of excess electrons on the μ_3-basic atoms in the compound's formula relative to the number of deficient electrons on the acidic atoms. We have adopted this arrangement in order to emphasize an important trend: for each acidic element, the acid goes from being underneutralized, to neutral, and finally to overneutralized as the number of basic electrons increases. We will return to the theme of matching the strengths of μ_3 acids and bases in optimizing phase stability in a later section of this Article. For now we will simply note that all of the phases in Figure 11 are united by a common theme. In each there is a net neutralization of the atoms involved. All of these phases can then be viewed as μ_3 acid/base

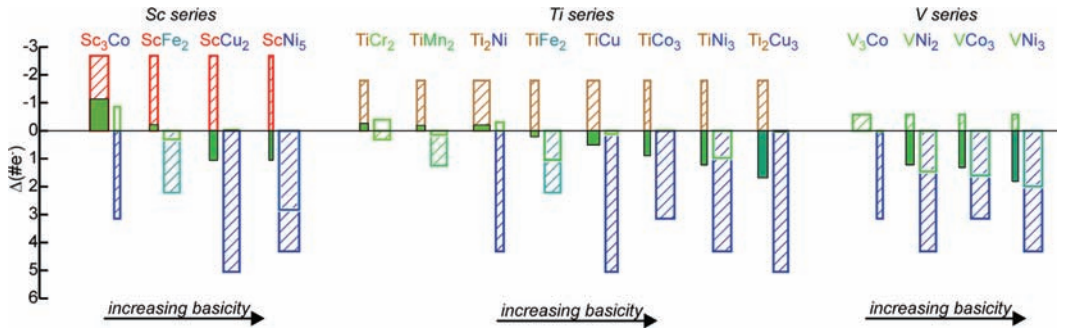

Figure 11. μ_3-Neutralization bar graphs for a selection of intermetallic phases chosen to sample the compositional and structural diversity of binary compounds forming between first-row transition metals. The compounds are grouped into three series based on the acid element: Sc, Ti, or V. Within each series, the compounds are arranged in order of increasing excess electrons per formula unit of the sublattice of the basic element; e.g., in Sc_3Co the Co sublattice has 3.0 excess electrons/Co × 1 Co = 2.1 excess electrons total that require neutralization, which is smaller than that of the Fe sublattice of $ScFe_2$ (2.1 electrons/Fe × 2 Fe = 4.2 excess electrons). The conventions of the bar graphs follow those given in the caption of Figure 9, except that here the thicknesses of the bars have been made proportional to the stoichiometric coefficient of the corresponding element in the formula for the compound. The areas of the bars then reflect the total number of excess or desired electrons on the basic and acidic sublattices of the phases. The structure types for the phases presented are: $CaCu_5$-type: $ScNi_5$; Al_3Os_2-type: Ti_2Cu_3; $MgZn_2$-type: $ScFe_2$, $TiFe_2$, $TiMn_2$; $MgCu_2$-type: $TiCr_2$; $AuCu_3$-type: $TiCo_3$; Al_3Ti-type: VNi_3; Al_3Pu-type: VCo_3; $MoSi_2$-type: $ScCu_2$, VNi_2; Cr_3Si-type: V_3Co; and eponymous structure types, the remaining phases.

dx.doi.org/10.1021/ic202727k | Inorg. Chem. 2012, 51, 4250−4264

adducts which (with varying degrees of success) have reduced the electron excess or deficiency of their component elements.

■ ORBITAL ORIGINS OF μ_3-NEUTRALIZATION

How does μ_3-neutralization arise in these examples of intermetallic phase formation? The simplicity of the Hückel Hamiltonian allows a transparent connection between the crystal structure of a phase and the DOS features related to μ_3 acidity. According to the relationships shown schematically in Figure 2, the moments of the electronic DOS link the shape of the DOS to structure by being expressible either as integrals over the DOS curve

$$\mu_n = \int_{-\infty}^{\infty} E^n \mathrm{DOS}(E)\, \mathrm{d}E \tag{8}$$

or as sums of products of Hamiltonian matrix elements

$$\mu_n = \sum_{i_1} \sum_{i_2} \cdots \sum_{i_n} \mathrm{H}_{i_1 i_2} \mathrm{H}_{i_2 i_3} \cdots \mathrm{H}_{i_n i_1} \tag{9}$$

The connection to geometry is contained in the mapping of the Hamiltonian matrix elements in the last equation to closed n-step paths through the structure. In our analysis of μ_3-acidity, we are principally interested in DOS curves for individual atoms, rather than for the full compound. This is achieved by limiting the first index, i_1, to include only orbitals on the atom of interest (AOI), i.e., $i_1 \in$ AOI. The remaining indices, i_2, i_3, ..., i_n, go over all orbitals in the basis set.

Upon standardizing the DOS curve to $\mu_1 = 0$, the above equations simplify substantially. When we limit our basis set for each atom to include a single degenerate set, such as the 3d orbitals on a Sc atom, $\mu_1 = 0$ for the DOS of the AOI is achieved by simply adjusting the zero of the energy axis so that $\mathrm{H}_{ii} = 0$ for that element. The diagonal matrix elements of the Hamiltonian matrix now measure on-site energies relative to this new reference point, rather than absolute ionization energies. As a consequence, *all products of Hamiltonian matrix elements involving in-place steps on atoms of the same element as the AOI are now zero.*

This greatly facilitates the geometrical decomposition of μ_3. μ_3 for an atomic DOS curve is calculated as the sum of the products of H_{ij}'s for closed 3-step paths beginning and ending on the AOI:

$$\mu_3 = \sum_{i_1 \in \mathrm{AOI}} \sum_{i_2} \sum_{i_3} \mathrm{H}_{i_1 i_2} \mathrm{H}_{i_2 i_3} \mathrm{H}_{i_3 i_1} \tag{10}$$

With $\mathrm{H}_{i_1 i_1} = 0$, only two geometrical features contribute to this summation: (1) 3-fold rings in which $i_1 \neq i_2 \neq i_3$, and (2) heteroatomic contacts, along which a closed 3-fold path can be constructed by stepping from the AOI to an atom of a different element ($\mathrm{H}_{i_1 i_2}$), stepping in place on that heteroatom ($\mathrm{H}_{i_2 i_2} \neq 0$), and then returning to the AOI ($\mathrm{H}_{i_2 i_1}$). Both are entirely focused on the first coordination sphere of the AOI, as it is not possible to venture further away from the AOI and still return using only three steps. Upon going from an elemental phase to an intermetallic compound, changes to the μ_3 sums may then be divided into two classes: changes in the 3-fold ring terms, and the introduction of the terms from heteroatomic contacts (which are of course absent in elemental phases).

These two types of changes may be probed separately by considering a hypothetical process by which the coordination environment of an atom in an elemental phase is gradually transformed to that of an intermetallic phase. We begin with an atom in an elemental phase. Then, in step 1, we change the atom's coordination environment to match the atomic positions of the intermetallic phase while leaving the elements unchanged, creating an elemental model of a binary compound. Changes in the μ_3 during this step of the transformation entirely reflect differences in coordination number and bond topology. Next, in step 2, we adjust the H_{ii} values of the positions corresponding to heteroatoms in the coordination environment to represent differences in ionization energy. This represents the introduction of terms for heteroatomic contacts into the μ_3 summation. Finally, in step 3, we complete the transformation to the intermetallic coordination environment by adjusting the H_{ij} values for the heteroatomic contacts according to the Wolfsberg–Helmholtz approximation.[117]

In Figure 12a, we apply this process to the formation of the CsCl-type ScCu phase from elemental Sc and Cu. Between pictures of the elemental and binary structures at the top and bottom of the panel, respectively, we show μ_3-acidity bar graphs

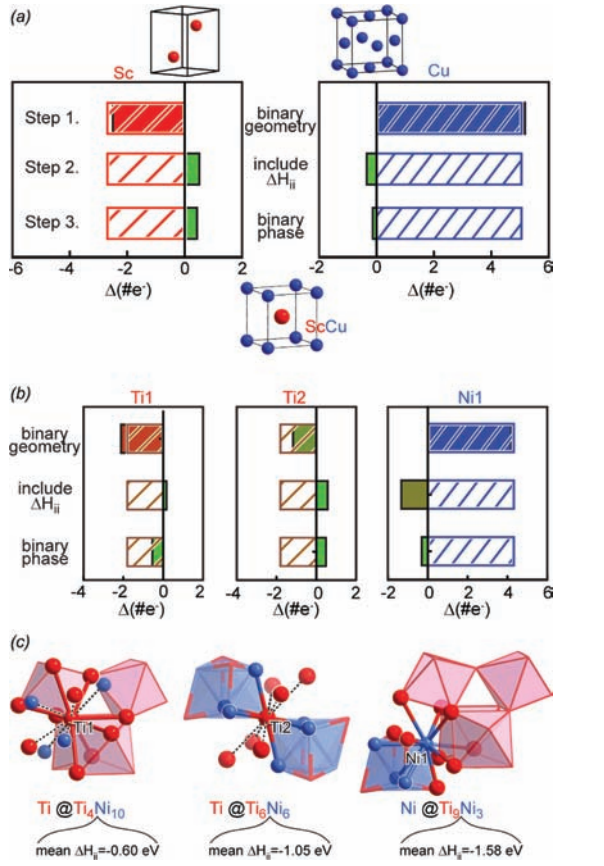

Figure 12. The orbital origin of μ_3-neutralization in ScCu and Ti_2Ni. (a) The μ_3 acidity differences for Sc (left) and Cu (right) are followed along a stepwise transformation from their elemental phases (striped bars) to their coordination environments in ScCu. Step 1: the coordination environments are changed to match that of the binary phase (without the introduction of heteroatoms). Step 2: the proper $\Delta\mathrm{H}_{ii}$ values are introduced into the coordination environments of Sc and Cu in the CsCl-type phase. Step 3: the remaining adjustments are made to complete the transformation to the ScCu phase. (b) The analogous process for each of the symmetry-distinct sites in Ti_2Ni. (c) The coordination environments of the symmetry distinct sites in Ti_2Ni, shown in the context of the structural motifs highlighted in Figure 1.

dx.doi.org/10.1021/ic202727k | Inorg. Chem. 2012, 51, 4250–4264

for each step of the transformation. On going from the coordination environments in their elemental phases to elemental models of their coordination environments in the binary phases (step 1), the bar for Sc shortens slightly while the Cu bar increases, but the change for both is fairly negligible. The electron counts for both remain far from the ideal. Upon introducing the proper ΔH_{ii} values into the coordination environment (step 2), a much larger change in the μ_3-acidity occurs. In fact, in the course of this step both Sc and Cu overshoot the ideal by a small degree. In completing the transformation to the binary coordination environments through adjustments of the H_{ij} values (step 3) a small change occurs as in step 1. In this final step, the bars have moved a little closer to the ideal.

This progression of μ_3-acidity values suggests that these steps are not of equal importance. The impact of the change in the coordination geometry (step 1) and the modifications of the interaction strengths along the interatomic contacts (step 3) are dwarfed by that of the introduction of differences in the onsite energies (step 2). In Figure 12b, the same breakdown is shown for each of the symmetry distinct sites in Ti_2Ni. Ti_2Ni is a much more complicated structure, marking a much more substantial change from the simple geometries of most elemental metals than ScCu. Despite this added complexity, the neutralization is again dominated by the introduction of the ΔH_{ii} terms. As is shown in the Supporting Information, we have performed similar analyses for a variety of transition-metal-based intermetallics. These results highlight the key role of the ΔH_{ii}'s (and, more generally, heteroatomic contacts) in μ_3-neutralization.

The large role played by the introduction of ΔH_{ii} values can be understood by reference to the most familiar of molecular orbital (MO) diagrams: that of two s-orbitals interacting to produce a bonding MO and an antibonding MO, as is shown in Figure 13. When the two s-orbitals are of the same energy (Figure 13a), each orbital contributes equally to the bonding and antibonding MOs. The projected DOS distributions for the two orbitals are then symmetric about the energy of the original, noninteracting orbitals, H_{ii}. The μ_3 value for both distributions is zero. When we introduce an H_{ii} difference between the two s-orbitals, this symmetry is lost (Figure 13b). The bonding MO now contains a larger contribution from the lower energy s-orbital, while the antibonding MO has a larger coefficient from the higher energy s-orbital. The resulting DOS distributions for the lower energy s-orbital are now weighted more heavily on the lower energy level; this corresponds to $\mu_3 > 0$. The DOS distribution for the higher energy s-orbital, on the other hand, has a larger weight on the higher energy level; i.e., its μ_3 value is negative.

These MO diagrams provide a specific example of a general rule: when H_{ii} differences are introduced between interacting atomic orbitals, the μ_3 value of the lower energy orbital will increase, leading to an increase in its ideal electron count. The μ_3 value for the higher energy orbital, conversely, decreases, with the ideal electron count likewise decreasing. This leads us to a general principle for μ_3-neutralization in transition-metal-based intermetallics that encompasses the μ_3-neutralization results that we have seen thus far. μ_3-Basic atoms, with their electron excess, are expected to be stabilized by replacing homoatomic interactions with heteroatomic ones with atoms with higher H_{ii} values (e.g., lower electronegativity). μ_3-Acidic atoms would then be stabilized by the introduction of atoms into their coordination environments with lower H_{ii} values

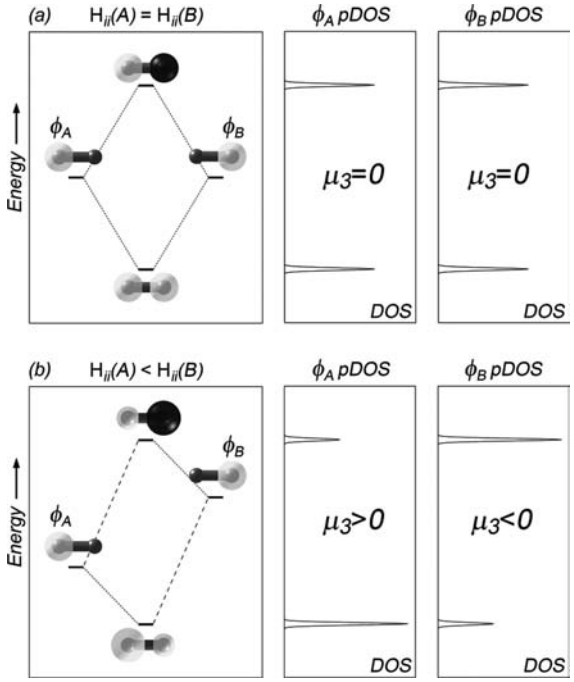

Figure 13. Influence of heteroatomic contacts on the μ_3 values of atomic DOS curves illustrated using diatomic molecules. (a) The interaction between two s orbitals with the same ionization energy leads to DOS curves for both orbitals that are symmetrically distributed between the bonding and antibonding levels ($\mu_3 = 0$). (b) The introduction of a difference in ionization energy increases the μ_3 value of the lower energy orbital, while decreasing that of the higher energy one.

(higher electronegativity). The most fortuitous interactions are then expected to arise in combinations between relatively electropositive μ_3-acids and relatively electronegative μ_3-bases.

IMPORTANCE OF MATCHING μ_3 ACID AND BASE STRENGTHS: STABILITY RANGE OF THE CsCl TYPE

Above, we saw that reacting elemental Sc and Cu to form ScCu almost completely neutralizes their μ_3-acidity and basicity. This was traced to the difference in H_{ii} for the 3d orbitals of these elements. The resulting connection between ΔH_{ii} for pairs of metals and the μ_3-neutralization arising from their reaction can be used to understand how the picture for ScCu is affected when Sc or Cu is replaced by a weaker μ_3-acid or base, respectively.

At the top of Figure 14, we show μ_3-neutralization graphs for a series of phases in which the Cu of ScCu is substituted by its neighbors to the left on the periodic table: ScNi, ScCo, ScFe, ScMn, and ScCr. Across this series two properties of the μ_3-basic metal change. First, the electron count of the elemental phase becomes closer to the μ_3-ideal (Figure 7); the μ_3-basicity thus decreases as we move left. Second, the electronegativity of the μ_3 base decreases, and as a consequence, the H_{ii} value of the 3d orbitals increases on going from Cu to Mn.

The μ_3-neutralization results for ScCu through ScCr reflect these changes in μ_3-basicity and H_{ii}. The largest effect is found for the neutralization of the μ_3 base. Elemental Cu is basic by 4.82 electrons/atom, and reaction with Sc leads to over-neutralization of 0.13 electrons. As we move from Cu to the weaker bases to its left, the large changes in μ_3-acidity upon interaction with Sc become increasingly overwhelming. The

dx.doi.org/10.1021/ic202727k | Inorg. Chem. 2012, 51, 4250–4264

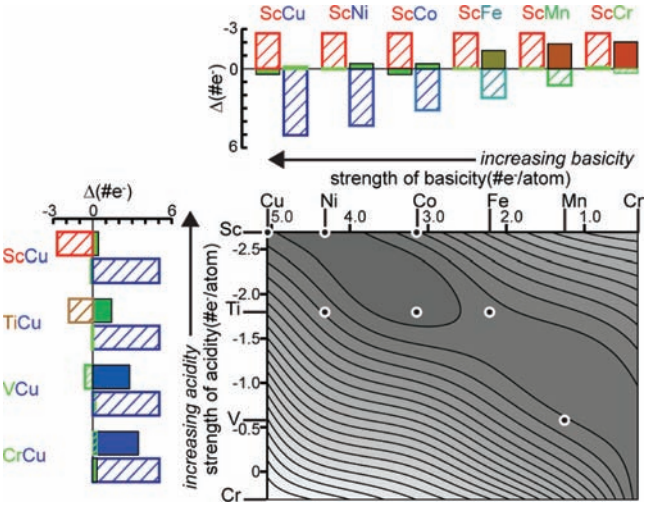

Figure 14. Contour map of the total residual μ_3-acidities calculated for CsCl-type phases formed between first-row transition metals, as a function of the μ_3-acidity of the elemental phases of the component acid (y-axis) and base (x-axis). Experimentally observed CsCl-type phases are indicated in the map with points.[37,96−116] Accompanying μ_3-neutralization bar graphs are given for the phases on the top and left edges of the map, to show trends in the neutralization as the Sc and Cu in ScCu are replaced with weaker acids and bases, respectively. Due to the small size of the data set, a cubic spline interpolation was used to smooth the map. The range of residual acidity values in the contour plot is 0.2 (dark gray) to 1.9 (light gray) electrons/atom.

overneutralization of 0.13 electrons for Cu in ScCu increases to 0.38 for Ni in ScNi, 0.83 for Co in ScCo, 1.37 for Fe in ScFe, 1.88 for Mn in ScMn, and 2.43 for Cr in ScCr. By the time we reach ScMn and ScCr, the degrees of overneutralization of Mn and Cr exceed their original basicities. In other words, the Sc becomes increasingly too strong of an acid for the μ_3-bases on moving from ScCu to ScCr.

These results can be correlated with experimental data on the existence of CsCl-type phases in binary systems between transition metals. CsCl-type phases are observed for ScCu, ScNi, and ScCo, while no such phase occurs in the Sc−Fe, Sc−Mn, or Sc−Cr systems. The nonexistence of ScFe, ScMn, and ScCr can be rationalized as due to the overneutralization of the Fe, Mn, and Cr. The effect of these substitutions is much smaller on the Sc; the large bandwidth of the Sc DOS distribution stemming from the diffuse nature of the Sc d orbitals means that the changes in the base H_{ii} are relatively unimportant.

We now try replacing Sc in ScCu with less acidic elements. The left side of Figure 14 presents μ_3-neutralization graphs for ScCu along with TiCu, VCu, and CrCu. Sc in ScCu is already overneutralized by 0.426 electrons/atom. The lower μ_3-acidity of Ti, V, and Cr causes this overneutralization to increase to 1.42 electrons/atom for Ti in TiCu, 2.80 for V in VCu, and 3.47 for Cr in CrCu. Just as Sc is too strong an acid for Cr, Mn, and Fe in the formation of CsCl-type phases, Cu is too strong a base for Ti, V, and Cr. In parallel with this increasing overneutralization of the acid is a small effect on the base: the lower H_{ii} values on moving from Sc to Cr leads to slight decreases in the neutralization of the Cu.

It seems that properly matching μ_3 acid and base strengths is essential for the formation of a CsCl-type phase between these metals. This is confirmed by μ_3-neutralization calculations on the remaining M1M2 (M1 = Sc, Ti, V, Cr; M2 = Cu, Ni, Co, Fe, Mn, Cr) CsCl-type structures. In Figure 14, we plot a structure map for this family with the μ_3-acidity of the M1 element plotted along the y-axis, and the μ_3-basicity of the M_2 metal along the x-axis. Dots are given in this map for experimentally observed CsCl-type phases. These cluster along the diagonal from ScCu to elemental Cr. Overlaid on this plot are contours corresponding to the average magnitude of the mismatch of the BF value for each atom from the μ_3-ideals, a quantity that may be termed the *average residual acidity* of the atoms, calculated for a CsCl-type phase for each M1−M2 pair. A valley of low residual acidity values can be perceived along the same diagonal that contains the observed phases. The structure map confirms that a poor degree of neutralization correlates well with the nonexistence of a CsCl-type compound.

These results complement earlier studies which trace the stability range of intermetallic CsCl-type phases to the valence electron concentration (VEC).[118] Each of the experimentally observed phases indicated in the map exhibit VEC values in the range 6−7 electrons per atom. The μ_3-acidity analysis interprets this result through the correlation of μ_3 acid and base strength with the group number of the element: taking a step to the left in the periodic table for the acid is countered by a step to right for the base.

RETURNING TO THE Ti−Ni SYSTEM, THIS TIME WITH μ_3-ACIDITY IN HAND

At the beginning of this Article, we attempted to illustrate the vast range of structures offered by intermetallic phases with a look at the diversity present in just one binary system, Ti−Ni. Having now developed a chemical picture for a driving force underlying the formation of these phases, we are now in a position to rationalize some of the structural aspects of the compounds in this system.

In Figure 15, we show μ_3-neutralization bar graphs for the Ti_2Ni, TiNi (CsCl-type), and $TiNi_3$ phases, below pictures of the corresponding structures. Let us start by considering the simplest of these compounds, TiNi, keeping in mind the guideline that the degree of μ_3-neutralization is determined by the balance in the strengths of homoatomic and heteroatomic interactions. TiNi's μ_3-neutralization bar graph (Figure 15b) indicates that its Ni atom are almost perfectly neutralized, while Ti is slightly overneutralized. This high degree of neutralization indicates that the Ti and Ni μ_3-acid/base strengths are well balanced. In observing this close balance, we might anticipate that changing the Ti/Ni ratio to form other compounds would tend to upset this neutralization, either by overshooting the perfect neutralization of the Ni through the incorporation of more Ti, or by deepening the overneutralization of the Ti through the addition of Ni.

One way by which such compounds can cope with these trends is through their choice of crystal structure. If we increase the Ti content by moving to the Ti_2Ni phase, we can expect that Ni will have to take on more Ti nearest neighbors as the ratio of Ti to Ni increases. In order to preserve the stability that Ni experiences in TiNi the Ni atoms in Ti_2Ni maximize their homoatomic contacts by clustering into Ni_4 tetrahedra (Figure 15a), with closer Ni−Ni distances arising here than in TiNi (2.8 vs 3.0 Å, respectively[86,119]). In this way, the Ni atoms essentially huddle back-to-back against overneutralization by the Ti majority. The result is that the Ni atoms in Ti_2Ni are only slightly overneutralized relative to TiNi, despite a doubling of the Ti content. The Ti atoms, on the other hand, take advantage of the higher availability of other Ti neighbors to

dx.doi.org/10.1021/ic202727k | Inorg. Chem. 2012, 51, 4250−4264

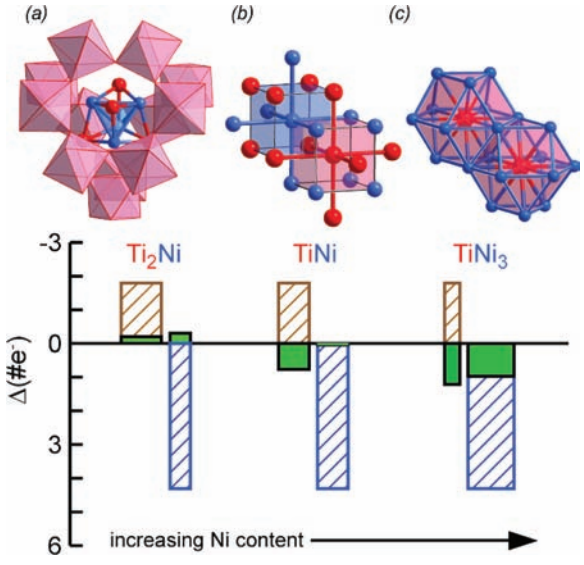

Figure 15. Structural trends within the Ti–Ni system viewed through the concept of μ_3-neutralization. μ_3-Neutralization bar graphs are given for the phases (a) Ti_2Ni, (b) TiNi, and (c) $TiNi_3$ below structural images of each phase. In TiNi, where the Ti/Ni ratio is equal to 1, Ti is moderately overneutralized while Ni has achieved essentially complete neutralization. Increasing the Ti content to create Ti_2Ni (a) would be expected to relieve the Ti overneutralization by adding more Ti–Ti contacts, but threatens to overneutralize the Ni through increased Ti–Ni interactions. The Ni atoms counter this by clustering into Ni_4 tetrahedra. Upon decreasing the Ti content from TiNi to obtain $TiNi_3$ (c), the smaller number of Ti atoms endangers the perfect neutralization of the Ni. To counter this, the Ni maximizes Ti–Ni contacts through exclusive occupancy of the Ti coordination environment, with a higher overneutralization being thrust upon the minority Ti atoms. See captions to Figures 9 and 11 for conventions used in the bar graphs.

form their own pyrochlore network, which allows the Ti to reduce its involvement with Ni relative to its coordination environment in TiNi.

If we move instead from TiNi to $TiNi_3$ where the base is the majority element, we would expect that Ni would need to maximize its contact with the Ti atoms in order to maintain as much of its neutralization as possible. The structure adopted is an hcp/fcc intergrowth where the first coordination sphere of Ti is entirely occupied by Ni, with no close Ti–Ti contacts being present (Figure 15c). The Ti atoms pay a price in this arrangement, with their overneutralization being increased over that in TiNi. However, as Ti is now outnumbered 3 to 1, the net neutralization for the phase is still positive.

In summary, the series of crystal structures observed across the Ti–Ni phase diagram can be rationalized as tuning the balance of Ti–Ti, Ni–Ni, and Ti–Ni interactions with changing composition in order to maximize the μ_3-neutralization of its elements. This conclusion has been reached through qualitative reasoning (of the kind used at the outset of many synthetic experiments), but with further developments using the Method of Moments a more quantitative foundation could be laid. We plan to illustrate this in an upcoming article tracing structural trends in intermetallics to the optimization of μ_3-acid/base interactions.

CONCLUSIONS

In this work, we have used the Method of Moments and DFT-calibrated Hückel calculations to extend the molecular bonding concept of Lewis acids and bases to the domain of intermetallic phases. In this generalization, we move from considering the donation and acceptance of whole electron pairs to the broader case of interactions between atoms with electron counts above or below the optimum, as determined from the μ_3 of the projected DOS curve. The result is categorization of elemental metals into μ_3 acids and bases, whose electron counts are below and above the μ_3 ideal, respectively. Using the first-row transition metals and the compounds formed between them as examples, we saw that the intermetallic phase formation frequently reduces these deviations for the atoms involved, and that the matching of the acid–base strength plays an important role in determining phase stability and structural preferences.

An important parallel emerges between Lewis acid–base adducts and intermetallic phases. In both classes of compounds, the acid–base interactions underlying them result in an enhanced separation in energy between filled bonding states and empty antibonding states. For Lewis acid–base adducts, this separation manifests itself in the form of a HOMO–LUMO gap, while in intermetallics it appears as a band gap or pseudogap in the electronic DOS states. However, whether the neutralization adopts the form of a gap between molecular energy levels or a minimum in a DOS curve, in both cases increased stability is a result. The enhanced oxidation resistance so frequently observed for intermetallic phases relative to their component elements can be rationalized along these lines.

The μ_3-acidity approach that has resulted from our analysis bears similarities and differences to the Zintl concept. Like the Zintl concept, the μ_3-acidity analysis overlays a bonding picture onto the geometrical features of a crystal structure. The two models approach bonding and their electron count requirements from different viewpoints. For Zintl phases, bonding pictures are built up from bonds and lone pairs, with the optimal electron counts being determined by the number of these features recognizable in the connectivities of the structures. μ_3 acidity instead examines how the cumulative impact of heteroatomic interactions sculpts an atom's projected DOS, without regard to the geometrical details of its coordination environment. This more diffuse view of orbital interactions is in line with the different degrees of bonding localization evident in Zintl phases and the less-polar intermetallics with which we have developed the μ_3 acid/base concept.

It will be interesting to see how these points of view merge as we attempt to apply μ_3 acidity analysis to increasingly more polar combinations of metals. Moving in this direction will require extending the μ_3 acidity concept beyond the transition-metal-based phases discussed in this Article. Generalizing the method is made challenging by the need for DOS curves that are well-described by their low order moments, μ_0–μ_4. This criterion is met well by the d-band-only models of the first-row transition metals, both in their elemental phases and in intermetallic phases. It is not met, however, by the d orbital projected DOS curves from DFT calculations, where interactions with the s and p orbitals lead to more complicated shapes. The method thus relies on a simple Hückel-type Hamiltonian involving a limited set of valence orbitals. In identifying such a set for, say, main group elements, one

dx.doi.org/10.1021/ic202727k | Inorg. Chem. 2012, 51, 4250–4264

encounters ambiguities. Should we consider the s and p orbitals of an element separately or as a combined set of valence orbitals? How much does the answer to this change from element to element, or from compound to compound? Providing answers to these questions will probably require a trial and error approach but has the potential to lead to a general theory of acid–base interactions that is applicable across the spectrum of inorganic compounds.

■ ASSOCIATED CONTENT

Supporting Information

Comparisons of the model DOS curves to those of GGA-DFT calculations, and detailed μ_3 neutralization data for each intermetallic phase discussed here. Detailed theoretical and computational procedures for the Hückel and DFT calculations, the refinement of Hückel parameters against DFT results, and the reconstruction of DOS curves from their moments. Tables of the DFT-calibrated Hückel parameter used. Derivations of eqs 5, 6, and 7. This material is available free of charge via the Internet at http://pubs.acs.org.

■ AUTHOR INFORMATION

Corresponding Author

*E-mail: danny@chem.wisc.edu.

Notes

The authors declare no competing financial interest.

■ ACKNOWLEDGMENTS

We gratefully acknowledge the financial support of the U.S. DOE Office of Science Early Career Program (DE-SC0003947) through the Office of Basic Energy Sciences, and the University of Wisconsin through start-up funds. This research involved calculations using computer resources supported by National Science Foundation Grant CHE-0840494.

■ REFERENCES

(1) Pearson, W. B. *The Crystal Chemistry and Physics of Metals and Alloys*; Wiley-Interscience: New York, 1972.
(2) Vegard, L. *Z. Phys.* **1921**, *5*, 17–26.
(3) Wang, C.; Hughbanks, T. *Inorg. Chem.* **1995**, *34*, 5524–5529.
(4) Kotur, B. Y.; Banakh, O. E.; Černý, R.; Espejel, J. V. P. *J. Alloys Compd.* **1997**, *260*, 157–161.
(5) Molina, L. M.; Alonso, J. A.; Stott, M. J. *Solid State Commun.* **1998**, *108*, 519–524.
(6) Guénée, L.; Yvon, K. *J. Alloys Compd.* **2003**, *356–357*, 114–119.
(7) Gòmez, C. P.; Lidin, S. *Phys. Rev. B* **2003**, *68*, 024203.
(8) Gòmez, C. P.; Lidin, S. *Chem.—Eur. J.* **2004**, *10*, 3279–3285.
(9) Ganguli, A. K.; Gupta, S.; Zhao, J.; Leon-Escamilla, E. A.; Corbett, J. D. *J. Solid State Chem.* **2005**, *178*, 2959–2972.
(10) Lukachuk, M.; Hoffmann, R. D.; Pöttgen, R. *Monatsh. Chem.* **2005**, *136*, 127–135.
(11) Dinges, T.; Rodewald, U. C.; Matar, S. F.; Eckert, H.; Pöttgen, R. *Z. Anorg. Allg. Chem.* **2009**, *635*, 1894–1903.
(12) Kohlmann, H.; Ritter, C. *Z. Anorg. Allg. Chem.* **2009**, *635*, 1573–1579.
(13) Lin, Q.; Corbett, J. D. *J. Am. Chem. Soc.* **2005**, *127*, 12786–12787.
(14) Lin, Q.; Corbett, J. D. *Philos. Mag.* **2006**, *86*, 607–613.
(15) Lin, Q.; Corbett, J. D. *J. Am. Chem. Soc.* **2006**, *129*, 13268–13273.
(16) Lin, Q.; Corbett, J. D. *J. Am. Chem. Soc.* **2007**, *129*, 6789–6797.
(17) Todorov, E.; Evans, M.; Lee, S.; Rousseau, R. *Chem.—Eur. J.* **2001**, *7*, 2652–2662.
(18) Jeitschko, W.; Parthé, E. *Acta Crystallogr.* **1967**, *22*, 417–430.
(19) Pearson, W. B. *Acta Crystallogr.* **1970**, *B26*, 1044–1046.
(20) Lu, G.; Lee, S.; Lin, J.; You, L.; Sun, J.; Schmidt, J. T. *J. Solid State Chem.* **2002**, *164*, 210–219.
(21) Fredrickson, D. C.; Lee, S.; Hoffmann, R. *Inorg. Chem.* **2004**, *43*, 6159–6167.
(22) Fredrickson, D. C.; Lee, S.; Hoffmann, R.; Lin, J. *Inorg. Chem.* **2004**, *43*, 6151–6168.
(23) Mott, N. F.; Jones, H. *The Theory of the Properties of Metals and Alloys*; Dover Publications, Inc.: New York, 1958.
(24) Fredrickson, D. C.; Lidin, S.; Venturini, G.; Malaman, B.; Christensen, J. *J. Am. Chem. Soc.* **2008**, *130*, 8195–8214.
(25) *Chemistry, Structure, and Bonding of Zintl Phases and Ions*; Kauzlarich, S. M., Ed.; VCH: New York, 1996.
(26) Sevov, S. In *Intermetallic Compounds: Principles and Practice Progress*; Westbrook, J. H., Ed.; Wiley-Blackwell: West Sussex, 2002; Vol. 3.
(27) *Zintl Phases: Principles and Recent Developments*; Fässler, T. F., Ed.; Springer: Heidelberg, 2011.
(28) Young, D. M.; Torardi, C. C.; Olmstead, M. M.; Kauzlarich, S. M. *Chem. Mater.* **1995**, *7*, 93–101.
(29) Xu, Z.; Guloy, A. M. *J. Am. Chem. Soc.* **1998**, *120*, 7349–7350.
(30) Nordell, K. J.; Miller, G. J. *Inorg. Chem.* **1999**, *38*, 579–590.
(31) Choe, W.; McWhorter, S.; Miller, G. J. *Z. Anorg. Allg. Chem.* **2002**, *628*, 1575–1580.
(32) Bobev, S.; Thompson, J. D.; Sarrao, J. L.; Olmstead, M. M.; Hope, H.; Kauzlarich, S. M. *Inorg. Chem.* **2004**, *43*, 5044–5052.
(33) You, T.-S.; Grin, Y.; Miller, G. J. *Inorg. Chem.* **2007**, *46*, 8801–8811.
(34) Corbett, J. D. *Inorg. Chem.* **2009**, *49*, 13–28.
(35) Bie, H.; Mar, A. *J. Solid State Chem.* **2009**, *182*, 3131–3137.
(36) The Ti–Ni system offers a wide range of functional materials, including shape memory alloys as well as candidates for hydrogen storage and catalysis. See: (a) Luan, B.; Cut, N.; Liu, H.; Zhao, H.; Dou, S. *J. Power Sources* **1994**, *52*, 295–299. (b) Fischer, T.; Kelemen, S.; Polizzotti, R. *J. Catal.* **1981**, *69*, 345–358.
(37) Le, D. H.; Colinet, C.; Hicter, P.; Pasturel, A. *J. Phys.: Condens. Matter* **1991**, *3*, 9965–74.
(38) Porter, D. A.; Easterling, K. E. *Phase Transformations in Metals and Alloys*; CRC Press: Boca Raton, FL, 1992.
(39) Hoffmann, R. *Solids and Surfaces: A Chemist's View of Bonding in Extended Structures*; VCH: New York, 1988.
(40) Pettifor, D. G. *Bonding and Structure of Molecules and Solids*; Clarendon Press/Oxford University Press: Oxford, 1995.
(41) Burdett, J. K. *Chemical Bonding in Solids*; Oxford University Press: New York, 1995.
(42) Berger, R. F.; Walters, P. L.; Lee, S.; Hoffmann, R. *Chem. Rev.* **2011**, *111*, 4522–4545.
(43) Hughbanks, T.; Hoffmann, R. *J. Am. Chem. Soc.* **1983**, *105*, 1150–1162.
(44) Hughbanks, T.; Hoffmann, R. *J. Am. Chem. Soc.* **1983**, *105*, 3528–3537.
(45) Dronskowski, R.; Blöchl, P. E. *J. Phys. Chem.* **1993**, *97*, 8617–8624.
(46) Becke, A. D.; Edgecombe, K. E. *J. Chem. Phys.* **1990**, *92*, 5397–5403.
(47) Savin, A.; Becke, A. D.; Flad, J.; Nesper, R.; Preuss, H.; von Schnering, H. G. *Angew. Chem., Int. Ed.* **1991**, *30*, 409–412.
(48) Savin, A.; Nesper, R.; Wengert, S.; Fässler, T. F. *Angew. Chem., Int. Ed.* **1997**, *36*, 1808–1832.
(49) Kohout, M. *Int. J. Quantum Chem.* **2004**, *97*, 651–658.
(50) Wagner, F. R.; Bezugly, V.; Kohout, M.; Grin, Y. *Theor. Chem. Acc.* **2007**, *13*, 5724–5741.
(51) Bader, R. F. W. *Chem. Rev.* **1991**, *91*, 893–928.
(52) Lewis, G. N. *Valence and the Structure of Atoms and Molecules*; The Chemical Catalog Company, Inc.: New York, 1923; pp 141–142.
(53) An analogy between the reactivity of transition metals toward intermetallic phase formation and the Lewis Theory of acids and bases was made in a different sense by Brewer and Wengert: Brewer, L.; Wengert, P. R. *Metall. Trans. B* **1973**, *4*, 83–104. In this work, metallic

elements are considered as Lewis acids when they have empty d orbitals able to accept an electron pair, and basic if they have filled non-bonding *d* orbitals in a position to donate an electron pair.
(54) Cyrot-Lackmann, F. *J. Phys. Chem. Solids* **1968**, *29*, 1235−1243.
(55) Cyrot-Lackmann, F. *J. Phys. Colloques* **1974**, *35*, 109−14.
(56) Burdett, J. K.; Lee, S. *J. Am. Chem. Soc.* **1985**, *107*, 3050−63.
(57) Hückel, E. *Z. Phys.* **1931**, *70*, 204−86.
(58) Hückel, E. *Z. Phys.* **1932**, *76*, 628−48.
(59) Haydock, R.; Heine, V.; Kelly, M. J. *J. Phys. C: Solid State Phys.* **1972**, *5*, 2845−2858.
(60) Gaspard, J. P.; Cyrot-Lackmann, F. *J. Phys. C: Solid State Phys.* **1973**, *6*, 3077−96.
(61) Haydock, R.; Heine, V.; Kelly, M. J. *J. Phys. C: Solid State Phys.* **1975**, *8*, 2591−2605.
(62) *The Recursion Method and Its Applications*; Pettifor, D. G., Weaire, D. L., Eds.; Springer-Verlag: Berlin, 1985.
(63) Burdett, J. K.; Lee, S. *J. Am. Chem. Soc.* **1985**, *107*, 3063−82.
(64) Cressoni, J. C.; Pettifor, D. G. *J. Phys.: Condens. Matter* **1991**, *3*, 495−511.
(65) Lee, S.; Rousseau, R.; Wells, C. *Phys. Rev. B* **1992**, *46*, 12121−31.
(66) Lee, S. *Annu. Rev. Phys. Chem.* **1996**, *47*, 397−419.
(67) Clark, P. M.; Lee, S.; Fredrickson, D. C. *J. Solid State Chem.* **2005**, *178*, 1269−1283.
(68) Carlsson, A. E. *Phys. Rev. B* **1991**, *44*, 6590.
(69) The condition that $\kappa = 0$ has this severe consequence on the shape of form DOS curve even when the values of higher order moments are considered. This can be seen in the continued fraction used in reconstructing the DOS curve from its moments (section S5 of the Supporting Information). Setting κ to zero leads to the termination of this continued fraction before information from higher moments is used.
(70) The first roots to an answer to this question can be found in the exploration the dependence of the total energy on the low order moments given by: Brown, R. H.; Carlsson, A. E. *Phys. Rev. B* **1985**, *32*, 6125−6130.
(71) Shohat, J. A.; Tamarkin, J. D. *The Problem of Moments*, 4th ed.; American Mathematical Society: Providence, 1970.
(72) Phillips, R.; Carlsson, A. E. *Phys. Rev. B* **1990**, *42*, 3345−3350.
(73) Seiser, B.; Hammerschmidt, T.; Kolmogorov, A. N.; Drautz, R.; Pettifor, D. G. *Phys. Rev. B* **2011**, *83*, 224116−1−224116−17.
(74) Nilsson, A.; Pettersson, L.; Norskov, J. *Chemical Bonding at Surfaces and Interfaces*; Elsevier Science: Amsterdam, 2007.
(75) Hückel calculations were performed using a slightly modified version of YAeHMOP: Yet Another extended Hückel Molecular Orbital Package, Version 3.0, by G. A. Landrum. See the Supporting Information for further details. YAeHMOP is freely available at http://sourceforge.net/projects/yaehmop/.
(76) GGA-DFT calculations were performed using the Vienna ab Initio similation package, as described in the Supporting Information. The computational methods employed are described in the following: (a) Kresse, G.; Furthmueller, J. *Phys. Rev. B* **1996**, *54*, 11169. (b) Kresse, G.; Furthmuller. *J. Comput. Mater. Sci.* **1996**, *6*, 15. (c) Bloechl, P. E. *Phys. Rev. B* **1994**, *50*, 17953. (d) Kresse, G.; Joubert, D. *Phys. Rev. B* **1999**, *59*, 1758.
(77) Young, D. A. *Phase Diagrams of the Elements*; University of California Press: Berkeley, 1991.
(78) In this work, we will focus on this original, descriptive definition of Lewis acids and bases, rather than later quantitative schemes such as in: Drago, R. S.; Wayland, B. B. *J. Am. Chem. Soc.* **1965**, *87*, 3571.
(79) This schematic diagram was created by considering two orbitals with $\Delta H_{ii} = 12$ eV with an interaction of $H_{ij} = -14.6$ eV.
(80) Chabot, B.; Parthé, E. *Acta Crystallogr., Sect. B* **1978**, *34*, 3173−3177.
(81) Pokatilov, V. S. *Phys. Solid State* **2001**, *43*, 1999−2002.
(82) Dwight, A. E.; Downey, J. W.; Conner, R. A. *Acta Crystallogr.* **1967**, *22*, 745−747.
(83) Braslavskaya, G. S.; Maslenkov, S. B. *Russ. Metall.* **1987**, *1*, 107−113.
(84) Johnson, J. R.; Reilly, J. J. *Inorg. Chem.* **1978**, *17*, 3103−3108.
(85) Yan, X.-L.; Chen, X.-Q.; Grytsiv, A.; Rogl, P.; Podloucky, R.; Schmidt, H.; Giester, G.; Ding, X.-Y. *Intermetallics* **2008**, *16*, 16−26.
(86) Mueller, M. H.; Knott, H. W. *Trans. Metall. Soc. AIME* **1963**, *227*, 674−678.
(87) Brown, P. J.; Deportes, J.; Ouladdiaf, B. *J. Phys.: Condens. Matter* **1992**, *4*, 10015−10024.
(88) Eremenko, V. N.; Buyanov, Y. I.; Prima, S. B. *Sov. Powder Metall. Met. Ceram.* **1966**, *5*, 494−502.
(89) Aoki, Y. *J. Phys. Soc. Jpn.* **1970**, *28*, 1451−1456.
(90) Laves, F.; Wallbaum, H. J. *Z. Kristallogr.* **1939**, *101*, 78−93.
(91) Schubert, K. *Z. Metallkd.* **1965**, *56*, 197−199.
(92) Waterstrat, R. M.; Dickens, B. *J. Appl. Phys.* **1974**, *45*, 3726−3728.
(93) Giessen, B. C.; Grant, N. J. *J. Less-Common Met.* **1965**, *8*, 114−119.
(94) Saito, S. *Acta Crystallogr.* **1959**, *12*, 500−502.
(95) Dasgupta, A.; Horton, J. A.; Liu, C. T. *High Temp. Alloys: Theory Des.* **1984**, 115−123.
(96) Markiv, V. Y.; Gavrilenko, I. S.; Pet'kov, V. V.; Belyavina, N. N. *Metallofizika (Akad. Nauk Ukr. SSR, Inst. Metallofiz.)* **1978**, *73*, 39−45.
(97) Semenova, E. L.; Rusetskaya, N. Y. *J. Alloys Compd.* **1997**, *262*−*263*, 258−262.
(98) Okamoto, H. In *Binary Alloy Phase Diagrams*, 2nd ed.; Massalski, T. B.; Okamoto, H.; Subramanian, P. R.; Kacprzak, L., Ed.; American Society for Metals: Materials Park, OH, 1990; Vol. *2*; pp 1235−1236.
(99) Okamoto, H. In *Binary Alloy Phase Diagrams*, 2nd ed.; Massalski, T. B.; Okamoto, H.; Subramanian, P. R.; Kacprzak, L., Ed.; American Society for Metals: Materials Park, 1990; Vol. *2*; pp 1767−1768.
(100) Okamoto, H. In *Binary Alloy Phase Diagrams*, 2nd ed.; Massalski, T. B.; Okamoto, H.; Subramanian, P. R.; Kacprzak, L., Ed.; American Society for Metals: Materials Park, OH, 1990; Vol. *2*; pp 2598−2600.
(101) Venkatraman, M.; Neumann, J. P. In *Binary Alloy Phase Diagrams*, 2nd ed.; Massalski, T. B.; Okamoto, H.; Subramanian, P. R.; Kacprzak, L., Ed.; American Society for Metals: Materials Park, OH, 1990; Vol. *2*; pp 1328−1330.
(102) Okamoto, H. *J. Phase Equilib.* **2002**, *23*, 549−550.
(103) Murray, J. L. In *Binary Alloy Phase Diagrams*, 2nd ed.; Massalski, T. B.; Okamoto, H.; Subramanian, P. R.; Kacprzak, L., Ed.; American Society for Metals: Materials Park, OH, 1990; Vol. *2*; pp 1250−1252.
(104) Dumitrescu, L. F. S.; Hillert, M.; Saunders, N. *J. Phase Equilib.* **1998**, *19*, 441−448.
(105) Murray, J. L. In *Binary Alloy Phase Diagrams*, 2nd ed.; Massalski, T. B.; Okamoto, H.; Subramanian, P. R.; Kacprzak, L., Ed.; American Society for Metals: Materials Park, OH, 1990; Vol. *3*; pp 2615−2617.
(106) Okamoto, H. *J. Phase Equilib.* **2002**, *23*, 382−383.
(107) Murray, J. L. In *Binary Alloy Phase Diagrams*, 2nd ed.; Massalski, T. B.; Okamoto, H.; Subramanian, P. R.; Kacprzak, L., Ed.; American Society for Metals: Materials Park, OH, 1990; Vol. *2*; pp 1500−1502.
(108) Smith, J. F.; Carlson, O. N.; Nash, P. G. In *Binary Alloy Phase Diagrams*, 2nd ed.; Massalski, T. B.; Okamoto, H.; Subramanian, P. R.; Kacprzak, L., Ed.; American Society for Metals: Materials Park, OH, 1990; Vol. *3*; pp 2880−2882.
(109) Smith, J. F. In *Binary Alloy Phase Diagrams*, 2nd ed.; Massalski, T. B.; Okamoto, H.; Subramanian, P. R.; Kacprzak, L., Ed.; American Society for Metals: Materials Park, OH, 1990; Vol. *2*; pp 1787−1791.
(110) Smith, J. F.; Carlson, O. N. In *Binary Alloy Phase Diagrams*, 2nd ed.; Massalski, T. B.; Okamoto, H.; Subramanian, P. R.; Kacprzak, L., Ed.; American Society for Metals: Materials Park, OH, 1990; Vol. *3*; pp 2620−2623.
(111) Kocherzhinskii, Y.; Vasilenko, V. *Russ. Metall.* **1985**, *2*, 186−188.

(112) Leonov, M. P.; Bochvar, N.; Ivanchenko, V. *Dokl. Phys. Chem.* **1986**, *290*, 886−887.
(113) Udovskii, A. L.; Kadyrzhanov, K. K.; Turkebaev, T. E. *Dokl. Akad. Nauk* **1993**, *331*, 431−438.
(114) Allibert, C. H.; Bernard, C.; Valignat, N.; Dombre, M. *J. Less-Common Met.* **1978**, *59*, 211−228.
(115) Totemeier, T. C.; Smithells, C. J. *Smithells Metals Reference Book*, 8th ed.; Butterworth-Heinemann: Oxford, U.K., 2004.
(116) Venkatraman, M.; Neumann, J. P. In *Binary Alloy Phase Diagrams*, 2nd ed.; Massalski, T. B.; Okamoto, H.; Subramanian, P. R.; Kacprzak, L., Ed.; American Society for Metals: Materials Park, OH, 1990; Vol. *2*; pp 1291−1292.
(117) Wolfsberg, M.; Helmholz, L. *J. Chem. Phys.* **1952**, *20*, 837−43.
(118) Yamashita, J.; Asano, S. *Prog. Theor. Phys.* **1972**, *48*, 2119−2131.
(119) Purdy, G. R.; Parr, J. G. *Trans. Metall. Soc. AIME* **1961**, *221*, 636−639.